International Journal of Mass Spectrometry 497 (2024) 117188

Contents lists available at ScienceDirect

International Journal of Mass Spectrometry

journal homepage: www.elsevier.com/locate/ijms

Gas-phase Ni(II) affinities of alternative metal binding peptides from competitive threshold collision-induced dissociation

Perfect Asare, Kwabena N. Senyah, Jonathan D. Wilcox, Jovany Morales, Laurence A. Angel *

Department of Chemistry, Texas A&M University-Commerce, 2600 S Neal Street, Commerce, TX, 75428, USA

ARTICLE INFO

Keywords:
Synapt TCID
Nickel(II) ternary complexes
IMAC
Ni(II) peptide tags

ABSTRACT

The Ni(II) affinity of the polyhistidine tag is used in the purification of recombinant proteins by immobilized metal affinity chromatography. Here we measured the relative gas-phase Ni(II) affinities of four alternative metal binding (amb) peptides and the 7xHis tag using the competitive threshold collision-induced dissociation (TCID) technique. The general primary structure of the four amb peptides was acetyl-Aa_1-Aa_2-Gly_3-Pro_4-Aa_5-Gly_6-Cys_7, designed to test whether the His_1-Cys_2 or Asp_1-His_2 would exhibit the higher Ni(II) affinity and whether the Tyr_5 with its ability of forming long-range π-nickel interaction and hydrogen bonding would contribute to the Ni(II) affinity. The Cys_7 is retained in all the amb sequences because previous research has shown that both the thiolate side group and carboxylate terminus simultaneously coordinate the metal ion. The Ni(II) affinity was measured using the dissociation of the [amb + Ni(II) + NTA]$^-$ complex, where NTA = nitrilotriacetic acid, which is a commonly used ligand for Ni(II) inside the IMAC column. The dissociation of [amb + Ni(II) + NTA]$^-$ produced two main product channels; [amb + Ni(II)]$^-$ + NTA and [NTA + Ni(II)]$^-$ + amb, whose competition was modeled by TCID to extract the relative gas-phase Ni(II) affinities. Extensive molecular modeling using PM6 located the low-energy structures whose molecular parameters were used in the TCID analyses if their collision cross sections agreed with those measured by traveling-wave ion mobility mass spectrometry and they were compatible with a concerted reaction. We compare the final results by conducting the TCID analyses using alternative PM6 parameters and by making the ternary complexes in acidic and basic solutions.

1. Introduction

Nickel(II) is the most common metal used in immobilized metal affinity chromatography (IMAC) in conjunction with the polyhistidine tag. However, the homogeneity of the polyhistidine tag can result in issues in the expressed recombinant protein's solubility and distribution in the host cell [1]. Moreover, the polyhistidine tag can affect the stability of the recombinant protein's conformation and disrupt its enzymatic or ligand binding activity [2]. A more diverse primary sequence of the peptide tag may be beneficial to the expression and stability of the recombinant protein. Here we present the results of a study of four heptapeptides (Fig. 1) with alternative metal binding (amb) sites and the 7xHis tag to determine their relative gas-phase Ni(II) affinities. These Ni(II) affinities were measured using competitive threshold collision-induced dissociation (TCID) and the study includes an evaluation of whether the TCID method can provide reliable measurements for these relatively large systems.

The competitive TCID technique was developed by Armentrout, Ervin and Rodgers [3–5] to measure the thermochemistry of competing reactions from the collisional activation and unimolecular dissociation of a complex and applied using the CRUNCH program [6]. The TCID technique was originally developed with guided ion beam tandem mass spectrometry instruments [7,8], but modified triple quadrupole instruments [9,10] have also been used. Recently, our group developed the TCID technique with the traveling-wave ion mobility-mass spectrometry (TWIMMS) instrument [11–13]. In the research presented here, the TCID technique is applied to derive Ni(II) affinities for the amb peptides (Fig. 1) and includes a revised analysis of the 7xHis peptide. The four amb peptides, **HCY**, **HCG**, **DHY** and **DHG** have the general primary structure acetyl-Aa_1-Aa_2-Gly_3-Pro_4-Aa_5-Gly_6-Cys_7, which tests how the His_1-Cys_2 or Asp_1-His_2 and Tyr_5 substituent groups effect the Ni(II) affinities. The Zn(II) affinities of **HCG** and **DHG** have been measured recently and showed that Zn(II) favored the His_1-Cys_2 [11]. Previous TWIMMS research has also monitored the "solution-phase" pH-dependent metal binding reactions of a wide variety of amb peptides [14–23], which showed for Zn(II) the preference for the amb His-2Cys

* Corresponding author.
E-mail address: Laurence.Angel@tamuc.edu (L.A. Angel).

https://doi.org/10.1016/j.ijms.2023.117188
Received 6 October 2023; Received in revised form 21 December 2023; Accepted 28 December 2023
Available online 30 December 2023

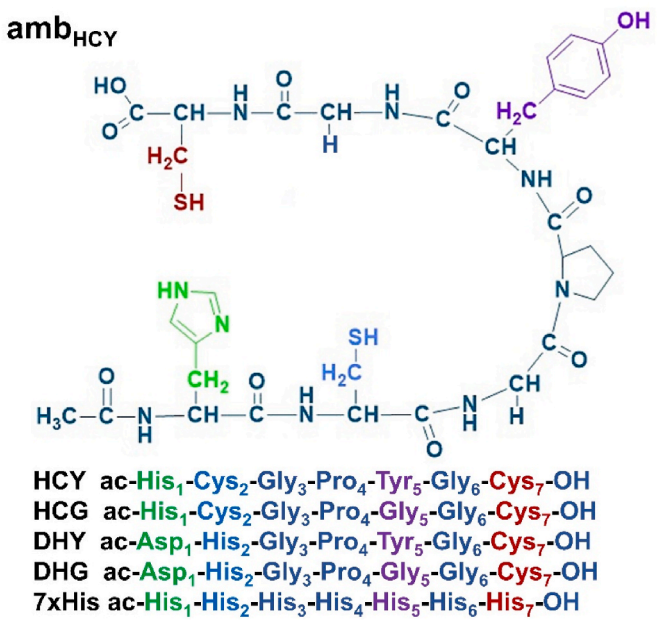

Fig. 1. The primary structures of the alternative metal binding (amb) peptides **HCY**, **HCG**, **DHY**, and **DHG** with the potential Ni(II) binding substituent sites in the first, second, fifth and last positions shown in green, blue, purple and red. The structure of the **7xHis** tag is also shown.

sites while Ni(II) preferred 2Asp-His [14]. The research here examines whether the gas-phase competitive TCID analyses of Ni(II) affinities will be in-line with these previous "solution-phase" studies. Moreover, the TCID analyses will test whether the tyrosyl, with its potential for forming π-nickel and hydrogen bonds, has an influence on the Ni(II) affinities. All the amb peptides (Fig. 1) have Cys_7 because our previous work showed its thiolate side group and carboxylate terminus can simultaneously coordinate the metal ion [11–13,19]. The effect of pH on the formation of the ternary complex was also tested to understand whether it influenced the competitive TCID analyses. The single negatively-charged [amb + Ni(II) + NTA]$^-$ complex, where NTA = nitrilotriacetic acid, has different possible binding sites for the Ni(II) from Asp, His, Cys, and carboxylate sites. Does the pH and pK_as' of these amb sites influence the formation of the ternary complex and the TCID analyses? Does a single conformer or ensemble of conformers exist in solution and retain their influence on the gas-phase TCID measurement? To try to answer these questions the ternary complex were made in acidic (pH 3) and basic solutions (pH 10) and using the TCID analyses the results were compared.

The TCID method required molecular parameters including rovibrational frequencies for the RRKM modeling of the dissociation of the activated complex through the orbiting transition states to the products [4]. A new molecular modeling technique was recently developed that used PM6 and DFTB/3OB_D4 geometry-optimizations and molecular dynamics simulations for locating these structures [11]. However, the full application of this method to triplet spin state Ni(II) complexes is unfeasible and here we used an extensive survey using semi-empirical PM6 to locate a series of low-energy conformers which also had collision cross sections (Ω_{He}), measured using the trajectory method with Lennard-Jones potentials (TMLJ), that agreed with the experimentally TWIMMS measured Ω_{He}. The overall negative charge of the [amb + Ni(II) + NTA]$^-$, [amb + Ni(II)]$^-$, and [NTA + Ni(II)]$^-$ complexes are due to the charge of Ni(II) and the loss of 3 protons from the neutral amb or NTA. The '−3H' is omitted from the formulas in the following manuscript, although we do discuss the protonation states of various complexes located by the PM6 method.

2. Experimental and computational methods

2.1. Reagents and sample preparation

The custom synthesis of the amb peptides **HCY**, **HCG**, **DHY**, and **DHG** was done by PepmicCo (http://www.pepmic.com/). Nickel(II) nitrate hexahydrate (99 % purity) was purchased from ACROS (https://www.acros.com/). Only deionized (DI) water 18 MΩ cm (http://www.millipore.com) and HPLC grade methanol (http://www.Fishersci.com/) solvents were used. Aqueous solutions of nickel(II) nitrate hexahydrate, NTA and amb were combined with dilution with DI water and HPLC methanol to final concentrations of 25:25:50 μM amb:Ni(II):NTA in a final 10 % methanol aqueous solution. The final pH of these solutions were pH 3 because of the acidic NTA. The same ratio of amb:Ni(II):NTA solutions were made at pH 10 by modifying the pH of the DI water using 9.4 mM ammonium acetate (ultrapure) and raising the pH using ammonium hydroxide (trace metal grade) (http://www.Fishersci.com/). All solutions were thoroughly mixed and left at room temperature for 10 min before TWIMMS analyses.

2.2. TWIMMS analyses

The Waters Synapt G1 instrument [24] (Fig. S1) was used for the analyses of the samples using the operating conditions described in the SI. The transmission quadrupole resolved the isotopic *m/z* peaks of the negatively-charged [amb + Ni(II) + NTA]$^-$ complex, which was focused into the trap cell and gated, via 200 μs voltage switch on the last lens of the trap, into the traveling-wave ion mobility (TW-IM) cell. The instrument uses argon gas in the trap and transfer cells and nitrogen in the TW-IM cell. In the TW-IM cell, the ternary complex underwent about 10,000 collisions with the N_2 buffer gas at 298 K, which thermalized the complex. The dissociation of [amb + Ni(II) + NTA]$^-$ was conducted in the transfer TW cell using predetermined collision energies (CE) that covered 0–100 % dissociation of the ternary complex and gave a series of energy-dependent product ions that were measured by the TOF *m/z* analyzer. The [amb + Ni(II) + NTA]$^-$ and the product ions were identified by their *m/z* isotope patterns and their arrival time distribution (ATD) alignment [11,12]. The ATD for each species were separated using Driftscope 2.0 and exported to MassLynx 4.1, where their areas were integrated to determine the relative intensities of each reactant and product at each collision energy. These procedures were repeated using three transfer argon gas pressures that covered the range 2–7 × 10^{-2} mbar, allowing the pressure dependence on multiple collisions to be extrapolated.

2.3. Collision cross sections

The TWIMMS Ω_{He} of [amb + Ni(II) + NTA]$^-$ and [amb + Ni(II)]$^-$ were measured using the quadrupole in non-resolving mode and the calibrants D-L polyalanine (PA). Although N_2 was used in the TW-IM cell, the calibration procedure used collision cross sections measured in helium (Ω_{He}) for the negatively-charged PA calibrants [25] to determine the Ω_{He} of the [amb + Ni(II) + NTA]$^-$ and [amb + Ni(II)]$^-$ complexes. The method is described in detail in the SI. The TWIMMS Ω_{He} allowed the selection of [amb + Ni(II) + NTA]$^-$ and [amb + Ni(II)]$^-$ conformers from the PM6 geometry-optimizations that had Ω_{He} measured using the trajectory method with Lennard-Jones (TMLJ) potentials from the IMOS program, that agreed with the TWIMMS Ω_{He} measurement [26].

2.4. PM6 molecular modeling

The study for locating low-energy, geometry-optimized structures of the [amb + Ni(II) + NTA]$^-$, [amb + Ni(II)]$^-$ and amb was accomplished using gas-phase structures with the semi-empirical PM6 [27] from the Gaussian09 program [28]. All initial structures contained only

trans-peptide bonds and their Asp, His, or Cys side groups and carboxyl groups were systematically arranged using GaussView 5 to test which final Ni(II) coordinations gave the lowest-energy structures. About 20–50 conformers of each species were located and their structures, electronic energies and TMLJ Ω_{He} were compiled and compared to the Ω_{He} measured by TWIMMS (Tables S1–S3).

2.5. Competitive threshold collision induced dissociation analyses

The voltages applied to the transfer cell were used directly as the lab-frame collision energies (E_{lab}) because ion current signal only decreased by 50 % when the transfer voltage was set to zero volts. For the TCID analyses, the E_{lab} were converted to center-of-mass collision energies (E_{cm}) using average masses of the argon (m_{Ar}) collision gas and the [amb + Ni(II) + NTA]$^-$ complex (m_C) as shown in equation S4. The E_{cm} is the maximum energy available for transfer to internal energy of the complex from a single collision between the complex and argon. The E_{cm}-dependent intensities of the product ions were converted to reaction cross sections using Beer's law as described previously [8,11].

The CRUNCH program [6] was used to model the E_{cm}-dependent reaction cross sections using the competitive threshold collision-induced dissociation (TCID) method. Competitive TCID [3–5] uses statistical RRKM theory to model the probability of the dissociation of the ternary complex through the excitation of its density of states and dissociation through the sum of states of the orbiting transition state (OTS) leading to products via their threshold energies. The total internal energy of the ternary complex E^* is described by its initial thermal energy plus the energy transferred upon collision with Ar, using the empirical deposition function shown in equation S5. The density and sum of states were calculated using the PM6 rovibrational frequencies from our selected conformers. No hindered rotors were used. The PM6 vibrational frequencies were scaled by the NIST recommended 1.062 scaling factor. In addition, for the OTS for the entropically favored [NTA + Ni(II)]$^-$ dissociation channel the vibrational frequencies <900 cm^{-1} where scaled by 0.70. Corrections are included for the kinetic shifts due to the limited time window that the complex must dissociate within so the products can be detected. For the TWIMMS the time window is 50 μs and is the average time ions take to pass from the transfer cell to the TOF mass analyzer [12]. The convoluted TCID modelling that fits the experimental data includes the 298 K temperature which effects the internal energy distribution of the [amb + Ni(II) + NTA]$^-$ complex [29], the distribution of translational energies of the Ar collision gas [7], and the integration over the total rotational angular momentum of the energized [amb + Ni(II) + NTA]$^-$ complex and the OTSs leading to products [30,31]. The OTSs are described by an ion-induced-dipole interaction of the dissociating products using dipole moments and polarizabilities from the PM6 calculations or NIST database for NTA.

The processes discussed above are included in equation (1) where the probability of dissociation and detection of the energized [amb + Ni(II) + NTA]$^-$ with total energy E^* into the product channel j is given by RRKM unimolecular reaction kinetics.

$$P_{D,\,j}(E^*,J) = k_j(E^*,J) \,/\, k_{tot.}(E^*,J)\,[1 - \exp(-k_{tot.}(E^*,J))\tau] \quad (1)$$

Here $k_{tot.} = \Sigma k_j$ is the total unimolecular dissociation rate constant of the channel j and τ is the 50 μs time window. J is the rotational angular momentum of the energized complex and the OTS for product channel j. The unconvoluted TCID model predicts the dissociation enthalpies of the ternary complex into the two product channels at 0 K and allows for the relative gas-phase Ni(II) affinities to be determined.

3. Results and discussion

3.1. The products reaction cross sections and transfer cell Ar gas pressure dependence

The reaction cross sections of the products from the dissociation of [**HCY** + Ni(II) + NTA]$^-$ and [**HCG** + Ni(II) + NTA]$^-$ are shown in Fig. 2. The [amb + Ni(II)]$^-$and [NTA + Ni(II)]$^-$ exhibited the lowest apparent threshold energies with [NTA-CO_2+Ni(II)]$^-$, which is the sequential loss of CO_2 from NTA, observed at higher energies. The difference in the apparent thresholds of [amb + Ni(II)]$^-$ and [NTA + Ni(II)]$^-$ is slightly greater from the dissociation of [**HCY** + Ni(II) + NTA]$^-$, which may indicate there is a significant effect from the inclusion of the tyrosyl group. The data was taken at three argon gas pressures to extrapolate the effect of multiple collisions and shows as the pressure *increased* from ~0.02 to 0.07 mbar the reaction cross sections exhibit a small *decrease* for all products observed. This behavior is consistent with multiple collisions removing some of internal excitation energy from the initial collision and partly deactivating the ternary complex.

The reaction cross sections of the products from the dissociation of [**DHY** + Ni(II) + NTA]$^-$ and [**DHG** + Ni(II) + NTA]$^-$ are shown in Fig. 3. The products [amb + Ni(II)]$^-$ and [NTA + Ni(II)]$^-$ exhibited the lowest apparent threshold energies but at higher energies the products [amb-H_2O + Ni(II)]$^-$, [NTA-CO_2+Ni(II)]$^-$, [amb-CO_2+Ni(II)]$^-$, and [amb-$C_3H_8O_2NS$ + Ni(II)]$^-$ were also observed. The loss of H_2O or CO_2 from [amb + Ni(II)]$^-$ originate from the Asp_1, a source of the oxygens and absent from the dissociation of **HCY** or **HCG** (Fig. 2). The loss of CO_2 and $C_3H_8O_2NS$, the latter being the loss of the Cys_7 residue, were *not* observed in our previous TCID studies of [amb + Zn(II) + NTA]$^-$ complexes of **HCG** and **DHG** [11–13].

3.2. PM6 modeling for locating conformers of [amb + Ni(II) + NTA]$^-$ and its dissociation products

The PM6 modeling results located a wide range of conformers of the [amb + Ni(II) + NTA]$^-$ and [amb + Ni(II)]$^-$ complexes (Tables S1 and S2). The [amb + Ni(II) + NTA]$^-$ conformers with the lowest electronic energies and whose TMLJ Ω_{He} agreed with the Ω_{He} measured by TWIMMS were selected to use in the TCID modeling (Table S3). For [amb + Ni(II)]$^-$, an extra criteria was that its conformation and Ni(II) binding coordination was compatible with a concerted dissociation of the selected [amb + Ni(II) + NTA]$^-$ conformer. Table 1 summarizes the TMLJ Ω_{He} of the final selected [amb + Ni(II) + NTA]$^-$ and [amb + Ni(II)]$^-$ conformers and compares them with the Ω_{He} measured by TWIMMS. The TCID analyses also required parameters for NTA, [NTA + Ni(II)]$^-$ and amb, whose TWIMMS Ω_{He} could not be measured, and the lowest-energy PM6 conformer from our work here or conformers we located in our previous studies were used [11–13]. The final selected conformers for the TCID modeling for **HCY**, **HCG**, **DHY**, **DHG** and **7xHis** are shown in Fig. 4, S2, S3, S4 and S5, respectively.

The PM6 conformer [**HCY** + Ni(II) + NTA]$^-$ exhibits octahedral coordination of the Ni(II) via the Cys_2, Cys_7 and the C-terminus, with two carboxylates (C_1 and C_2) and nitrogen (N) from NTA (Fig. 4). The three negatively charged sites of three carboxylates and the 2+ charge of Ni(II) gives the ternary complex its overall −1 charge. For [**HCY** + Ni(II)]$^-$, the Ni(II) is coordinated via His_1, Cys_2, Cys_7 and C-terminus. The conformer for [**HCY** + Ni]$^-$ was selected not only because of its PM6 energy and Ω_{He} but also because it maintains the same Ni(II) binding sites as the ternary complex and is compatible with a concerted reaction mechanism described by an OTS. These structures also indicated that the dissociation mechanism proceeds via two proton transfers from the two Cys to the two carboxylates of NTA, and with the His_1 they displaced the NTA from coordinating Ni(II).

The ternary [amb + Ni(II) + NTA]$^-$ complexes of **HCG**, **DHY**, and **DHG** also exhibited Ni(II) coordination by two carboxylates and nitrogen from NTA and either Cys, Asp or C-terminus sites. The [amb + Ni

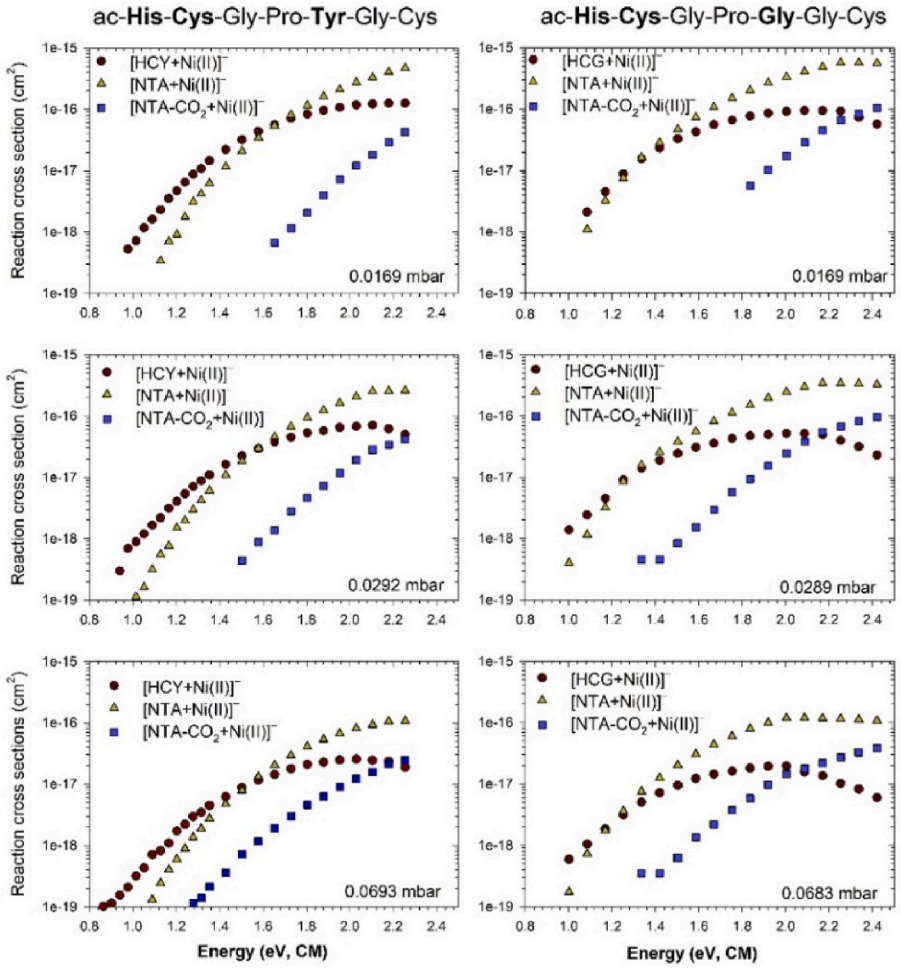

Fig. 2. The reaction cross sections of the products [amb + Ni(II)]$^-$, [NTA + Ni(II)]$^-$ and [NTA-CO_2+Ni(II)]$^-$ from the dissociation of [**HCY** + Ni(II) + NTA]$^-$ (left panel) and [**HCG** + Ni(II) + NTA]$^-$ (right panel) using three argon gas pressures between 0.02 and 0.07 mbar.

(II)]$^-$ complex typically exhibited Ni(II) coordination via His, Cys, Asp and C-terminus sites (Figs. S2, S3, S4). The PM6 sum of electronic and zero-point energies (HF) of the selected conformers with the predicted PM6 enthalpy changes, ΔH_0, for the two dissociation reactions are shown in Table S3.

3.3. Threshold collision-induced dissociation analyses

The E_{cm}-dependent, reaction cross sections recorded at the three pressures (Figs. 2 and 3) were converted by a linear extrapolation to a zero Ar gas pressure to obtain reaction cross sections at a single collision limit. The comparison of the resulting reaction cross sections for the two main dissociation channels from **HCY** and **HCG** are shown in Fig. S6 and for **DHY** and **DHG** in Fig. S7. The competitive TCID analyses used the PM6 rovibrational frequencies to describe the energized [amb + Ni(II) + NTA]$^-$ complex and the PM6 rovibrational frequencies, dipole moments and polarizabilities to describe the two loose orbiting transition states using those of [amb + Ni(II)]$^-$ + NTA or [NTA + Ni(II)] + amb products. The exception was NTA whose dipole moment and polarizability was taken from NIST. This reaction model implied two competing concerted reactions without activation barriers in excess to the energy of the products, where the 0 K threshold energies, E_1 and E_2, are equal to the reaction dissociation enthalpies of reactions 2 and 3.

$$[\text{amb} + \text{Ni(II)} + \text{NTA}]^- \rightarrow [\text{amb} + \text{Ni(II)}]^- + \text{NTA} \quad (2)$$

$$[\text{amb} + \text{Ni(II)} + \text{NTA}]^- \rightarrow [\text{NTA} + \text{Ni(II)}]^- + \text{amb} \quad (3)$$

A comparison of the located TCID fits that were used to measure the relative gas-phase Ni(II) affinities with the fitting parameters N and σ_0 from the energy deposition function (eq S5), and entropies of activation ΔS_0 at 1000 K for reactions (2) or (3) are shown in Table S4.

Fig. 5 shows a selection of results where the solid lines are the competitive TCID fits that reproduced the experimental reaction cross sections and included the convolution over the translational or internal energy distributions available at 298 K. The unconvoluted TCID cross sections (not shown) predicted the 0 K dissociation enthalpies, ΔH_0, for reactions 2 and 3 and are shown in Fig. 5. The difference in the ΔH_0 for reactions 2 and 3, *i.e.*, $\delta\Delta_{Ni}H_0 = \Delta H_0(2) - \Delta H_0(3) = \Delta_{Ni}H_0(\text{amb}) - \Delta_{Ni}H_0(\text{NTA})$, provides the relative gas-phase Ni(II) affinities for the four amb species.

Table 2 (middle column) shows the mean and 95 % confidence interval of the relative Ni(II) affinities derived from multiple fits to the reaction cross sections and includes the reevaluated competitive TCID analyses of **7xHis** (Fig. S8). The previous TCID analysis of **7xHis** used separate threshold fits of the two products, whereas, here the competitive TCID method that includes explicit treatment of the competitive shifts inherent in multiple channels is used with new parameters from the conformers [**7xHis** + Ni(II) + NTA]$^-$, [**7xHis** + Ni(II)]−and **7xHis** shown in Fig. S5. The first derived Ni(II) affinity shown for each species in Table 2 are those obtained using the parameters from the conformers shown in Fig. 4, S2, S3, S4, and S5 with the details of the individual fits shown in Table S4. Table 2 also includes Ni(II) affinities derived from using parameters from alternative conformers of [amb + Ni(II) + NTA]$^-$ selected from Tables S5 and S6 and shown in Figs. S9 and S10. The Ni(II)

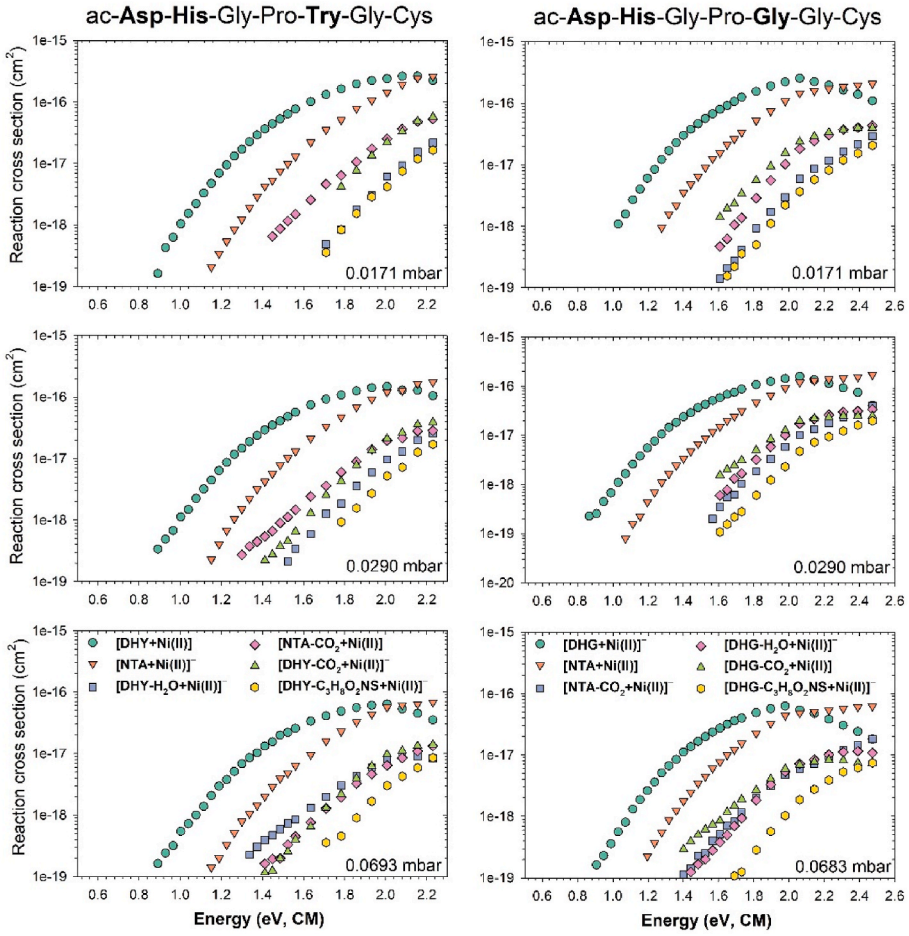

Fig. 3. The reaction cross sections of the products [amb + Ni(II)]$^-$, [NTA + Ni(II)]$^-$, [amb-H_2O + Ni(II)]$^-$, [NTA-CO_2+Ni(II)]$^-$, [amb-CO_2+Ni(II)]$^-$, and [amb-$C_3H_8O_2NS$ + Ni(II)]$^-$ from the dissociation of [**DHY** + Ni(II) + NTA]$^-$ (left panel) and [**DHG** + Ni(II) + NTA]$^-$ (right panel) using three argon gas pressures between 0.02 and 0.07 mbar.

Table 1
Comparison of the TMLJ Ω_{He} (Å^2) of the lowest-energy stationary states located by PM6 geometry-optimizations that agreed with those measured by TWIMMS Ω_{He} and compatible with a concerted reaction mechanism. The PM6 conformers are shown in Fig. 4, S2, S3, S4 and S5.

amb	[amb + Ni(II) + NTA]$^-$		[amb + Ni(II)]$^-$	
	PM6 TMLJ[a]	TWIMMS[a]	PM6 TMLJ	TWIMMS
HCY	211	211	187	188
HCG	200	195	175	173
DHY	208	206	189	188
DHG	201	192	172	172
7xHis	239	241	224	219

[a] The Ω_{He} measurements have approximate relative uncertainties of 2 %.

affinities shown in Table 2 in the last row in italics are derived from the mean and 95 % confidence interval of multiple fits using two sets of parameters for the [amb + Ni(II) + NTA]$^-$ complex.

Overall the results in Table 2 suggest Ni(II) affinities are in the order **DHG > 7xHis ≥ DHY > HCY > HCG** indicating the preference of Ni(II) for the Asp_1-His_2 substituent groups over His_1-Cys_2. The greater Ni(II) affinity of **DHG** over **DHY**, indicates the tyrosyl does not contribute to the Ni(II) affinity, which is consistent with the PM6 conformer of [**DHY** + Ni(II)]$^-$ (Fig. S3), whose tyrosyl is displaced from the rest of the molecule. However in contrast, the greater Ni(II) affinity of **HCY** over **HCG** does indicate a tyrosyl contribution with the [**HCY** + Ni(II)]$^-$ conformer in Fig. 4 showing the out-of-plane π-orbitals of the tyrosyl ring approximately orientated towards the Ni(II) and a hydrogen bond from the hydroxyl to the sulfur of Cys_7. However, the evaluation of the choice of conformers to use in the TCID analyses in the following sections shows that this outcome is sensitive to the choice of conformers.

3.4. pH-dependence on the threshold collision-induced dissociation analyses

Previous research of the amb peptides has shown that using electrospray of different pH solutions allowed the pH-dependent metal binding behaviors to be monitored by TWIMMS, which was especially useful for negative ions as they reproduced the solution-phase charge states and the expected solution-phase reactivity based on the p*K*as' of His and Cys [15–23]. The TCID results discussed above were all derived from the ternary complexes made in pH 3 solutions because of the acidic NTA. To check whether pH could influence the formation of different conformers of the ternary complexes and whether the TCID method could detect this, the ternary complexes of **HCG** and **DHG** were made again but in solutions of pH 10 and the resulting reaction cross sections are compared to those measured from the pH 3 solutions in Figs. S11 and S12, respectively. The located TCID fits that were used to measure the relative gas-phase Ni(II) affinities of the ternary complexes made at pH 10, with the fitting parameters N and σ_0 from eq S5, and entropies of activation ΔS_0, are shown in Table S7. Typical examples of the TCID fits that reproduced the reaction cross sections of the products from the ternary complexes made at pH 10 are shown in Fig. 6.

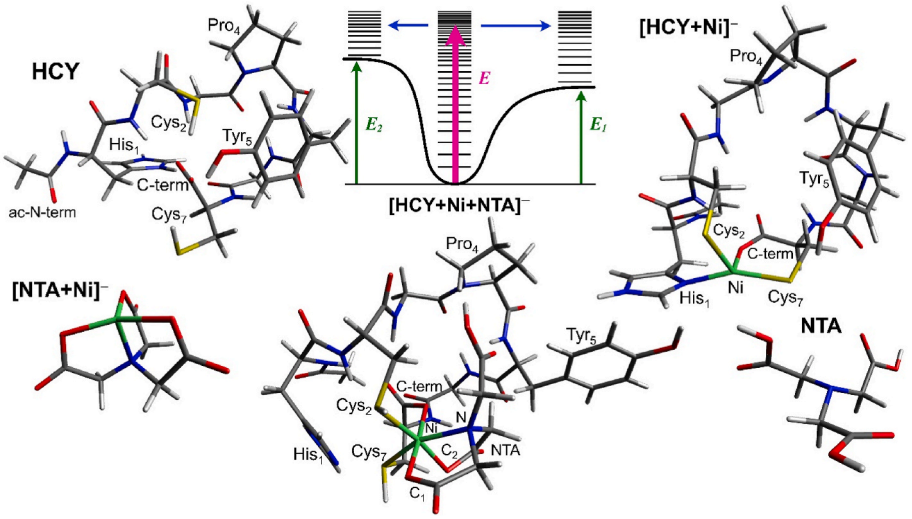

Fig. 4. The PM6 molecular structures of the [**HCY** + Ni(II) + NTA]$^-$ ternary complex and its products [**HCY** + Ni(II)]$^-$ + NTA (right) and [NTA + Ni(II)]$^-$ + **HCY** (left). Their PM6 rovibrational frequencies were used to calculate the density of states of the [**HCY** + Ni(II) + NTA]$^-$ complex and the sum of states of the orbiting transition states as illustrated in the representative potential energy surface. The [**HCY** + Ni(II) + NTA]$^-$ was chosen based on its PM6 electronic energy predicting it was the most stable conformer that also had a TMLJ collision cross sections (Ω_{He}) that agreed with the experimentally measured TWIMMS Ω_{He} (Table 1). The [**HCY** + Ni(II)]$^-$ complex was selected based on it being the most stable PM6 conformer that retained the Cys_2, Cys_7 and C-terminus Ni(II) binding sites as the ternary complex and also included His_1 binding site that replaced the NTA.

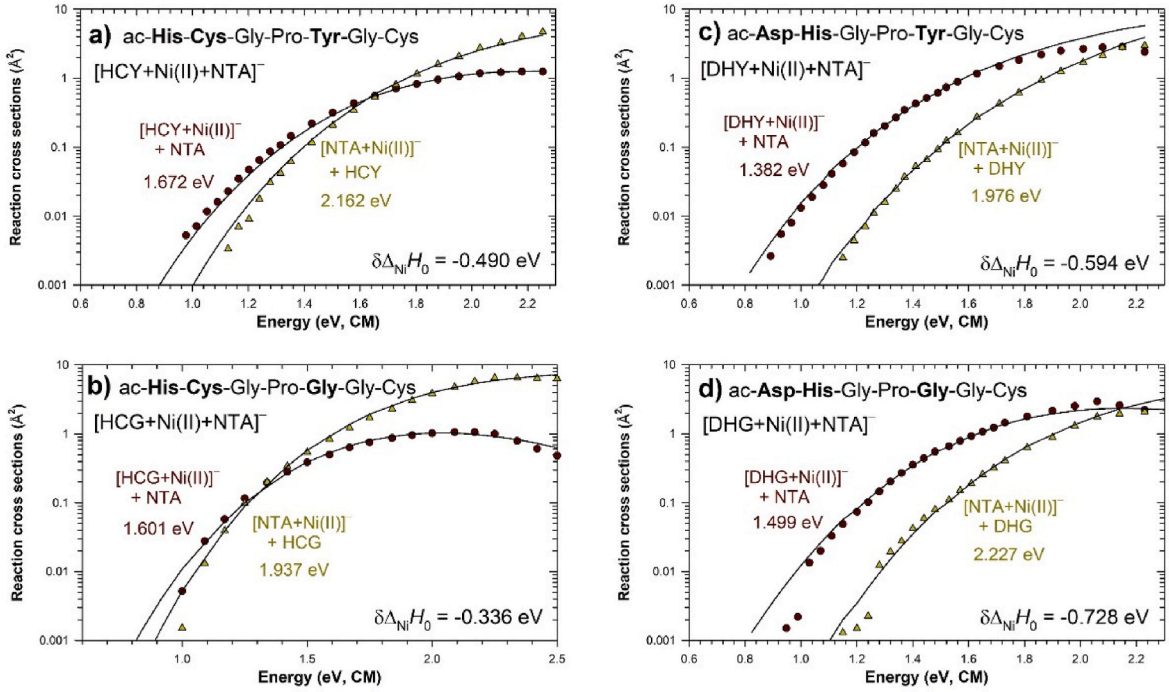

Fig. 5. The convoluted TCID fits (black lines) to the experimental reaction cross sections of [amb + Ni(II)]$^-$ (brown circles) and [NTA + Ni(II)]$^-$ (green triangles) from **a)** [**HCY** + Ni(II) + NTA]$^-$, **b)** [**HCG** + Ni(II) + NTA]$^-$, **c)** [**DHY** + Ni(II) + NTA]$^-$ and **d)** [**DHG** + Ni(II) + NTA]$^-$ made in pH 3 solutions. The values are the 0 K dissociation enthalpies, ΔH_0, of reactions 2 and 3 and $\delta\Delta_{Ni}H_0$ provides the relative gas-phase Ni(II) affinities as described in the text.

*3.5. Using different [**HCG** + Ni(II) + NTA]$^-$ conformers for the TCID analyses of pH 3 and pH 10*

Table 2 (column 3) shows the Ni(II) affinities from the fits of the pH 10 data with different [**HCG** + Ni(II) + NTA]$^-$. Using the molecular parameters from the conformers shown in Fig. S2, the selection of TCID fits that reproduced the reaction cross sections gave $\delta\Delta_{Ni}H_0 = -0.417 \pm 0.022$ eV, which is not significantly different from the Ni(II) affinity -0.361 ± 0.036 at pH 3 because of the overlapping error bars. However, the ternary complexes were made at different pH, which could relate to the TCID of two different conformers of the ternary complex. Considering the p*K*as of NTA and **HCG** (Table S8), the three most likely negatively charged sites are the two carboxylates from NTA and the C-terminus from **HCG**, with His deprotonated and neutral, giving the overall −1 charge state of the [**HCG** + Ni(II) + NTA]$^-$ conformer shown in Fig. S2. The electronic energies and TMLJ Ω_{He} of the PM6 conformers located for [**HCG** + Ni(II) + NTA]$^-$ are shown in Table S5 with the values in bold indicating the selected conformers used in the TCID

Table 2
Comparison of the relative gas-phase Ni(II) affinities determined from the TCID method. Ni(II) affinities in bold are from selected [**DHG** + Ni(II) + NTA]$^-$ or [**HCG** + Ni(II) + NTA]$^-$conformers that resulted in Ni(II) affinities that were significantly different at the 95 % confidence level between the pH 3 and pH 10 measurements. Details of the individual fits are shown in Tables S4 and S7.

Primary structure	pH 3, $\delta\Delta_{Ni}H_0$ (eV)	pH 10, $\delta\Delta_{Ni}H_0$ (eV)
ac**Asp**-**His**-Gly-Pro-**Gly**-Gly-Cys	**−0.726 ± 0.018** [a]	**−0.631 ± 0.012** [a]
	–	−0.681 ± 0.028 [b]
	−0.687 ± 0.034 [b]	−0.708 ± 0.028 [b]
	−0.703 ± 0.027 [c] (8)	*−0.672 ± 0.030* [c] (12)
acHis-His-His-His-His-His-His	−0.633 ± 0.019 [a]	–
	−0.626 ± 0.018 [c] (6)	–
ac**Asp**-**His**-Gly-Pro-**Tyr**-Gly-Cys	−0.599 ± 0.040 [a]	–
	−0.598 ± 0.009 [c] (6)	–
ac**His**-**Cys**-Gly-Pro-**Tyr**-Gly-Cys	−0.489 ± 0.033 [a]	–
	−0.485 ± 0.012 [c] (6)	–
ac**His**-**Cys**-Gly-Pro-**Gly**-Gly-Cys	−0.361 ± 0.036 [a]	**−0.417 ± 0.022** [a]
	−0.370 ± 0.011 [b]	−0.403 ± 0.021 [b]
	–	−0.384 ± 0.028 [b]
	−0.355 ± 0.016 [c] (8)	*−0.398 ± 0.014* [c] (12)

[a] The mean and 95 % confidence interval of $\delta\Delta_{Ni}H_0$ derived from four fits using different energy ranges that reproduced the reaction cross sections using the PM6 molecular parameters from structures in Fig. 4, S2, S3, S4 and S5 and two fits obtained after changing the vibrational frequencies of the energized complex and the two orbiting transition states by ±10 %.

[b] Same as in footnote 1 but with the [amb + Ni(II) + NTA]$^-$ replaced with an alternative conformer selected from Table S5 or S6 and shown in Fig. S9 or Fig. S10.

[c] The mean and 95 % confidence intervals of $\delta\Delta_{Ni}H_0$ derived from the multiple fits using different energy ranges and changing the PM6 parameters of different conformers of [amb + Ni(II) + NTA]$^-$ as discussed in the text. In brackets the number of TCID fits used to calculate the mean and standard deviation.

analyses. The first value shown in bold are for the conformer shown in Fig. S2. Table S5 also shows a 22 kJ/mol higher energy conformer with same Ni(II) binding sites: Cys_2H, Cys_7H, COO^-, N, 2 COO^-, but with a more compact structure (TMLJ Ω_{He} = 196 Å^2), which agrees more precisely with the TWIMMS measured Ω_{He} = 195 Å^2 (Table 1). This conformer, shown in Fig S9a, is also compatible with the concerted reaction using the two OTS (Fig. S2) and resulted the TCID analysis of the pH 10 data giving $\delta\Delta_{Ni}H_0 = -0.403 \pm 0.021$ eV (Table 2), which is not significantly different from the result of the pH 3 data. However, conformer **S9a** was also used as an alternative complex in modeling the pH 3 data, resulting with $\delta\Delta_{Ni}H_0 = -0.370 \pm 0.011$ eV (Table 2), which because of the smaller error bars *was* significantly different from the −0.417 ± 0.022 eV for the pH 10 data measured using only the conformers shown in Fig. S2.

One more [**HCG** + Ni(II) + NTA]$^-$ conformer was selected from Table S5 based on it having four negatively-charged Ni(II) binding sites; Cys_2^-, Cys_7H, COO^-, N, 2 COO^-, with His_1 protonated as imidazolium (Fig. S9b), and its TMLJ Ω_{He} agreeing with TWIMMS. However, using this **S9b** conformer with the two OTS used previously with the TCID model for the pH 10 data gave $\delta\Delta_{Ni}H_0 = -0.384 \pm 0.028$ eV (Table 2), which was not significantly different from the pH 3 results. Therefore, only by using the conformers shown in Fig. S2 for pH 10, but for pH 3 replacing the ternary complex with the more compact conformer **S9a**, were the Ni(II) affinities significantly different. Deriving the Ni(II) affinities from the mean and 95 % confidence interval using energy fits of all the [**HCG** + Ni(II) + NTA]$^-$ conformers used in either the analyses of pH 3 or pH 10 data (Tables 2, S4 and S7) also resulted in significantly different Ni(II) affinities of −0.355 ± 0.016 eV (pH 3) and −0.398 ± 0.014 eV (pH 10).

3.6. Using different [*HCG* + *Ni(II)*]$^-$ conformers for the TCID analyses of pH 3 and pH 10

The [**HCG** + Ni(II)]$^-$ conformer used for the OTS, shown in Fig. S2, has Ni(II) binding sites of Cys_2^-, Cys_7^-, and COO^- terminus and was selected based on its TMLJ Ω_{He} = 175 Å^2 that agreed with the TWIMMS = 173 Å^2 as shown in bold in Table S9. However, a lower energy conformer with His_1, Cys_2^-, Cys_7^-, and COO^- terminus coordination of Ni (II) (Table S9, Fig. S13a) was also located, but with a smaller TMLJ Ω_{He} = 163 Å^2. Including **S13a** in the TCID analyses of the pH 10 data to describe the OTS of reaction 2 with the parameters from the other 4 conformers shown in Fig. S2, resulted in an increased Ni(II) affinity, −0.580 ± 0.010 eV, of **HCG** (Table 3). This higher Ni(II) affinity is related to the smaller entropy of activation for reaction 2 (Tables 3 and S7) because of the more ordered structure of **S13a** over the original [**HCG** + Ni(II)]$^-$ conformer used from Fig. S2.

The analyses above shows the choice of the [**HCG** + Ni(II)]$^-$ conformer used for the TCID analyses significantly affects the final Ni(II) affinity. For the Ni(II) affinities shown in Table 2, all the [amb + Ni(II)]$^-$ complexes apart from **HCG** had four Ni(II) binding sites. For consistency, the analyses of the pH 3 data for **HCG** was conducted again using the conformers shown in Fig. S2 but with the [**HCG** + Ni(II) + NTA]$^-$ conformer replaced with the conformer shown in Fig. S9a and the [**HCG** + Ni(II)]$^-$ conformer replaced for the conformer shown in Fig. S13a. The results in Table 4 show using these conformers gave a significantly higher −0.553 ± 0.010 eV Ni(II) affinity for **HCG**, although still significantly lower than the Ni(II) affinity from the reevaluation of **HCG** at pH 10 (Table 3), but higher than the Ni(II) affinity of **HCY** at pH 3 (Table 2).

3.7. Using different [*DHG* + *Ni(II)* + *NTA*]$^-$ conformers for the TCID analyses of pH 3 and pH 10

For **DHG**, consideration of the p*K*as' (Table S8) showed the most likely negatively charged sites are the two carboxylates of NTA and the

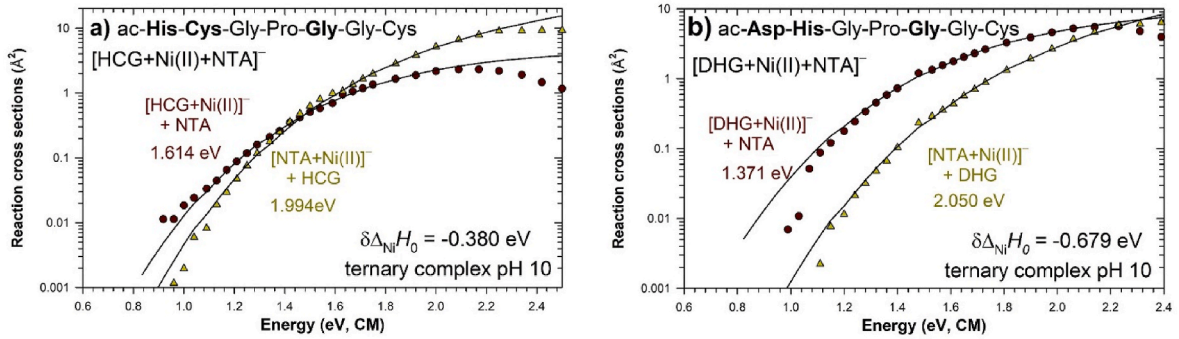

Fig. 6. The convoluted TCID fits (black lines) to the experimental reaction cross sections of [amb + Ni(II)]$^-$ (brown circles) and [NTA + Ni(II)]$^-$ (green triangles) from **a)** [**HCG** + Ni(II) + NTA]$^-$ and **b)** [**DHG** + Ni(II) + NTA]$^-$ made in pH 10 solutions. The values are the 0 K dissociation enthalpies, ΔH_0, of reactions 2 and 3 and $\delta\Delta_{Ni}H_0$ provides the relative gas-phase Ni(II) affinities as described in the text.

Table 3
The located TCID fits that were used to measure the relative gas-phase Ni(II) affinity of **HCG** at pH 10 with the new conformer **S13a**, with the fitting parameters N and σ_0 from equation S(5), and entropies of activation ΔS_0 (J/(mol K)) at 1000 K for reactions (2) or (3).

Primary structure	pH 10, $\delta\Delta_{Ni}H_0$ (eV)	N	σ_0 (Å^2)	$\Delta S_0(2)$	$\Delta S_0(3)$
ac**His**-**Cys**-Gly-Pro-**Gly**-Gly-Cys	**−0.580 ± 0.010**[a]	–	–	137	580
Ni(II) sites: Cys_2H, Cys_7H, COO^- term N, $2COO^-$ TMLJ = 200 Å^2	−0.592	0.82	55.7		
Ni(II) sites: His_1, Cys_2^-, Cys_7^-, COO^- term TMLJ = 163 Å^2	−0.578	1.27	59.2		
Varied parameters ±10 %	−0.574	1.42	62.0		
	−0.578	1.38	59.4		
	−0.592	*1.02*	*65.1*		
	−0.568	*1.64*	*65.6*		

[a] The mean and 95 % confidence interval of $\delta\Delta_{Ni}H_0$ derived from six fits that reproduced the reaction cross sections using the PM6 molecular parameters from structures in Fig. S2, but with the [amb + Ni(II)]$^-$ replaced with the alternative conformer selected from Table S9, and shown in Fig. S13a.

Table 4
The located TCID fits that were used to measure the relative gas-phase Ni(II) affinity of **HCG** at pH 3 with the conformers **S9a** and **S13a**, with the fitting parameters N and σ_0 from equation S(5), and entropies of activation ΔS_0 (J/(mol K)) at 1000 K for reactions (2) or (3).

Primary structure	pH 3, $\delta\Delta_{Ni}H_0$ (eV)	N	σ_0 (Å^2)	$\Delta S_0(2)$	$\Delta S_0(3)$
ac**His**-**Cys**-Gly-Pro-**Gly**-Gly-Cys	**−0.553 ± 0.010**[a]	–	–	162	605
Ni(II) sites: Cys_2H, Cys_7H, COO^- term N, $2COO^-$ TMLJ = 196 Å^2	−0.565	0.91	30.7		
Ni(II) sites: His_1, Cys_2^-, Cys_7^-, COO^- term TMLJ = 163 Å^2	−0.564	0.92	30.8		
Varied parameters ±10 %	−0.562	1.00	32.6		
	−0.560	1.10	36.1		
	−0.502	*1.42*	*29.8*		
	−0.567	*1.01*	*28.9*		

[a] The mean and 95 % confidence interval of $\delta\Delta_{Ni}H_0$ derived from six fits that reproduced the reaction cross sections using the PM6 molecular parameters from structures in Fig. S2, but with [**HCG** + Ni(II) + NTA]$^-$ replaced with the conformer **S9** and [amb + Ni(II)]$^-$ replaced with the conformer **S13a**.

Asp_1 carboxylate side group and the C-terminus, with the His side group protonated as imidazolium. This was the charge state of the [**DHG** + Ni(II) + NTA]$^-$ conformer used in the original TCID analyses of the complex made at pH 3 (Table 2, Fig. S4). Using the conformers shown in Fig. S4 for the TCID fitting of the pH 10 data gave $\delta\Delta_{Ni}H_0$ = −0.631 ± 0.012 eV (Table 2), which is significantly smaller than the TCID result at pH 3 using the same conformers. The electronic energies and TMLJ Ω_{He} of the PM6 conformers located for [**DHG** + Ni(II) + NTA]$^-$ (Table S6) shows that all the conformers located had larger TMLJ Ω_{He} than those measured by TWIMMS Ω_{He} = 192 Å^2. The lowest energy conformer used in the first TCID analyses had one of the smallest TMLJ Ω_{He} = 201 Å^2 (Fig. S4). The second conformer selected in bold (Table S6) was 37 kJ/mol higher in energy and had Ni(II) binding sites of Asp_1H, Cys_7H, COO^- term, N, $2COO^-$ and exhibited TMLJ Ω_{He} = 200 Å^2. This conformer (Fig. S10a) was compatible with the same two OTS used previously and gave $\delta\Delta_{Ni}H_0$ = −0.681 ± 0.028 eV (Table 2), with overlapping error bars with the −0.726 ± 0.018 eV result at pH 3. One other conformer with TMLJ Ω_{He} = 196 Å^2 was used (Table S6) because it was in the best agreement with the TWIMMS Ω_{He} = 192 Å^2. This conformer had Ni(II) binding sites of Asp_1^-, Cys_7^-, N, $2COO^-$ (Fig. S10b) and gave $\delta\Delta_{Ni}H_0$ = −0.708 ± 0.028 eV for the pH 10 data, and −0.687 ± 0.034 eV for the pH 3 data (Table 2). These results are not significantly different from each other or with the other Ni(II) affinity measurements for **DHG** shown in Table 2, apart from the pH 10 $\delta\Delta_{Ni}H_0$ = −0.631 ± 0.012 eV measurement. Deriving the Ni(II) affinities from the fits using all the different [**DHG** + Ni(II) + NTA]$^-$ conformers for the pH 3 or pH 10 data (Tables 2, S4 and S7) were also not significantly different. Therefore, only the competitive TCID analyses using the conformers in Fig. S4 or Fig. S10b resulted in the pH 3 and pH 10 data giving Ni(II) affinities that were significantly different and predicted the Ni(II) affinity of **DHG** was greater at pH 3 than at pH 10.

3.8. Using different [*DHG* + Ni(II)]$^-$ conformers for the TCID analyses of pH 3 and pH 10

To check how the choice of parameters for the OTS of reaction 2 affected the Ni(II) affinity of **DHG**, a different [**DHG** + Ni(II)]$^-$ conformer was selected from Table S10 for the pH 3 analyses that exhibited Asp_1^-, Cys_7^-, COO^- terminus Ni(II) binding sites and shown in Fig. S13b. This conformer replaced the [**DHG** + Ni(II)]$^-$ conformer shown in Fig. S4 and its parameters were used in the TCID analyses with those of the other conformers of Fig. S4. The results in Table 5, shows the Ni(II) affinity of **DHG** significantly decreased when compared to those derived previously (Table 2), which is related to the increase in the entropy of activation (Tables 5 and S4) for reaction 2 because the [**DHG** + Ni(II)]$^-$ conformer has one less Ni(II) binding site and is more disordered than the conformer from Fig. S4.

3.9. Comparison of Ni(II) and Zn(II) binding modes in peptides

The overall results from this study show that the highest Ni(II) affinities were determined when the [amb + Ni(II)]$^-$ complex had 4 Ni(II) coordination sites, which were the His_1, Cys_2^-, Cys_7^-, COO^- term for **HCY** and **HCG** and Asp_1^-, His_2, Cys_7^-, COO^- term for **DHY** and **DHG**. If the [amb + Ni(II)]$^-$ complex with these 4 coordination sites were included in the TCID analyses the inclusion of tyrosyl ring *decreased* the Ni(II) affinity, so the Ni(II) affinities followed the order **DHG > 7xHis ≥ DHY ≥ HCG > HCY**. The analyses shows the two amb peptides with the substituent sites of Asp_1-His_2-Cys_7 and the 7xHis tag had the greatest Ni(II) affinities. This compared with our previous competitive TCID research which investigated the Zn(II) affinities of **HCG** and **DHG** and showed the His_1-Cys_2-Cys_7 sequence had the higher Zn(II) affinity [11].

Table 5
The located TCID fits that were used to measure the relative gas-phase Ni(II) affinity of **DHG** at pH 3 using the [**DHG** + Ni(II)]$^-$ conformer **S13b**, with the fitting parameters N and σ_0 from equation S(5), and entropies of activation ΔS_0 (J/(mol K)) at 1000 K for reactions (2) or (3).

Primary structure	pH 3, $\delta\Delta_{Ni}H_0$ (eV)	N	σ_0 (Å^2)	$\Delta S_0(2)$	$\Delta S_0(3)$
ac**Asp**-**His**-Gly-Pro-**Gly**-Gly-Cys	0.535 ± 0.046[a]	–	–	214	632
Ni(II) sites: Asp_1^-, Cys_7H, COO^- term, N, $2COO^-$ TMLJ = 201 Å^2	−0.519	1.65	30.5		
Ni(II) sites: Asp_1^-, Cys_7^-, COO^-	−0.517	1.61	29.6		
TMLJ = 176 Å^2	−0.522	1.64	29.7		
Varied parameters by ±10 %	−0.518	1.69	31.8		
	−0.511	*1.60*	34.1		
	−0.625	*0.78*	65.7		

[a] The mean and 95 % confidence interval of $\delta\Delta_{Ni}H_0$ derived from six fits that reproduced the reaction cross sections using the PM6 molecular parameters from structures in Fig. S4 but with the [amb + Ni(II)]$^-$ replaced with the alternative conformer selected from Table S10, and shown in Fig. S13b.

Overall these findings agreed with our previous TWIMMS pH-dependent "solution-phase" research that showed Zn(II) had the preference of forming complexes with amb peptides that contained at least 2 Cys sites, whereas, Ni(II) had the preference of forming ternary complexes with those with 2–3 Asp sites [14]. Nickel(II) and Zn(II) binding studies reported by other groups include multi-histidine peptides [32–34], Cys containing peptides [35,36], and mixed Asp and Cys hexapeptides [37,38]. However, these peptides, which are based on sequences found in proteins, typically result in Ni(II) binding modes that are principally affected by the square planar chelation via multiple deprotonated amine groups from the peptide backbone and not affected by multiple binding by the Asp, His or Cys side groups. For example, the study of the His containing peptide fragments of the human prion protein indicated different Ni(II) binding preferences at the various His sites but in all cases the Ni(II) was coordinated via His and 3 deprotonated backbone amine groups [39]. For the amb peptides studied here with His in the first or second position, the His and 3 backbone amine coordination is disrupted by the central Pro_4 residue and Ni(II) and Zn(II) are typically coordinated via the available side groups of His, Cys or Asp and the C-terminus, which are suitably positioned to interact simultaneously with the metal ion [14,16,17]. An earlier study of Zn(II) chelation by terminally blocked tripeptides containing Cys and/or His side groups at both termini with a central Pro residue predicted chelation was via the two side groups [40]. The article reported stability constants (log β) for the 2His variety of 3.29 that increased for Cys/His to 5.61 and again for 2Cys to 9.31, showing that the Cys thiolate binding of Zn(II) was higher than that of His imidazole. These results are in agreement with our research comparing Zn(II) and Ni(II) binding by the amb peptides [14].

4. Conclusions

This research investigated the dissociation reactions of ternary complexes of the type $[amb + Ni(II) + NTA]^-$, where the amb peptides had the general primary structure acetyl-$\mathbf{Aa_1}$-$\mathbf{Aa_2}$-Gly_3-Pro_4-$\mathbf{Aa_5}$-Gly_6-Cys_7 (Fig. 1) and used alternative Ni(II) interaction sites in the first, second and fifth positions. Using the competitive TCID analyses from the CRUNCH reaction dynamics program [6] the relative gas-phase Ni(II) affinities for the four amb peptides were measured. Overall the results from this study showed the Ni(II) affinities follow the order **DHG > 7xHis ≥ DHY ≥ HCG > HCY**, if the $[amb + Ni(II)]^-$ conformer used in the TCID analyses had Ni(II) binding sites of His_1, Cys_2^-, Cys_7^-, COO^- term for **HCY** and **HCG** and Asp_1^-, His_2, Cys_7^-, COO^- term for **DHY** and **DHG**.

The differences of the TCID measurements of the Ni(II) affinities of **HCG** and **DHG** from the ternary complexes made in either acidic and basic solutions, where only significantly different when specific conformers of the $[amb + Ni(II) + NTA]^-$ ternary complex or $[amb + Ni(II)]^-$ were used. For **HCG** the selection of conformers of $[\mathbf{HCG} + Ni(II) + NTA]^-$ and $[\mathbf{HCG} + Ni(II)]^-$ gave significantly different Ni(II) affinities of -0.580 ± 0.010 eV (pH 10, Table 3) and -0.553 ± 0.010 eV (pH 3, Table 4), with the greater Ni(II) affinity at pH 10 for **HCG**. This can be attributable to the p*K*as' of His_1-Cys_2 making them more efficient at binding Ni(II) at higher pH.

For **DHG** there was also a significant difference in the TCID measured Ni(II) affinities when the same conformers were used in both analyses -0.726 ± 0.018 eV (pH 3, Table 2) and -0.631 ± 0.012 eV (pH 10, Table 2), which gave a higher Ni(II) affinity for pH 3. This may be attributable to the inclusion of Asp_1 whose relatively low p*K*a allows it to efficiently bind Ni(II) and out compete other potential sites at lower pH.

CRediT authorship contribution statement

Perfect Asare: Data curation, Formal analysis, Investigation. **Kwabena N. Senyah:** Data curation, Formal analysis, Methodology. **Jonathan D. Wilcox:** Data curation, Formal analysis, Investigation. **Jovany Morales:** Data curation, Formal analysis, Investigation. **Laurence A. Angel:** Conceptualization, Data curation, Formal analysis, Funding acquisition, Investigation, Methodology, Project administration, Resources, Software, Supervision, Validation, Visualization, Writing – original draft, Writing – review & editing.

Declaration of competing interest

The authors declare that they have no known competing financial interests or personal relationships that could have appeared to influence the work reported in this paper.

Data availability

Data will be made available on request.

Acknowledgements

This work was supported by the National Science Foundation (2247511), NSF REU program (CHE-1659852), NSF instrument support (MRI-0821247), and Welch Foundation (T-0014). We thank Kent M. Ervin (University of Nevada - Reno) and Peter B. Armentrout (University of Utah) for sharing the CRUNCH program.

Appendix A. Supplementary data

Supplementary data to this article can be found online at https://doi.org/10.1016/j.ijms.2023.117188.

References

[1] C. Amarasinghe, J.-P. Jin, The Use of affinity tags to Overcome Obstacles in recombinant protein expression and purification, Protein Pept. Lett. 22 (2015) 885–892.
[2] K.A. Majorek, M.L. Kuhn, M. Chruszcz, W.F. Anderson, W. Minor, Double trouble-Buffer selection and His-tag presence may be responsible for nonreproducibility of biomedical experiments, Protein Sci. 23 (2014) 1359–1368.
[3] P.B. Armentrout, K.M. Ervin, M.T. Rodgers, Statistical rate theory and kinetic energy-resolved ion Chemistry: theory and applications, J. Phys. Chem. A 112 (2008) 10071–10085.
[4] M.T. Rodgers, P.B. Armentrout, Statistical modeling of competitive threshold collision-induced dissociation, J. Chem. Phys. 109 (1998) 1787–1800.
[5] M.T. Rodgers, K.M. Ervin, P.B. Armentrout, Statistical modeling of collision-induced dissociation thresholds, J. Chem. Phys. 106 (1997) 4499–4508.
[6] P.B. Armentrout, K.M. Ervin, CRUNCH, Fortran Program, 2016 version 5.2002.
[7] K.M. Ervin, P.B. Armentrout, Translational energy dependence of Ar+ + XY → ArX + + Y (XY = H2,D2,HD) from thermal to 30 eV c.m, J. Chem. Phys. 83 (1985) 166–189.
[8] V.F. DeTuri, P.A. Hintz, K.M. Ervin, Translational activation of the SN2 Nucleophilic Displacement reactions Cl- + CH3Cl (CD3Cl) → ClCH3 (ClCD3) + Cl-: a guided ion beam study, J. Phys. Chem. A 101 (1997) 5969–5986.
[9] D. Gatineau, A. Memboeuf, A. Milet, R.B. Cole, H. Dossmann, Y. Gimbert, D. Lesage, Experimental bond dissociation energies of benzylpyridinium thermometer ions determined by threshold-CID and RRKM modeling, Int. J. Mass Spectrom. 417 (2017) 69–75.
[10] V. Romanov, U.H. Verkerk, C.K. Siu, A.C. Hopkinson, K.W. Siu, Threshold collision-induced dissociation measurements using a ring ion guide as the collision cell in a triple-quadrupole mass spectrometer, Anal. Chem. 81 (2009) 6805–6812.
[11] K.N. Senyah, P. Asare, J.D. Wilcox, F. Angiolari, R. Spezia, L.A. Angel, Extending the competitive threshold collision-induced dissociation of Zn(II) ternary complexes using traveling-wave ion mobility-mass spectrometry, Int. J. Mass Spectrom. 488 (2023) 117041.
[12] A.J. Corrales, A.V. Arredondo, A.A. Flores, C.L. Duvak, C.L. Mitchell, R. Spezia, L. A. Angel, Thermochemical Studies of Ni(II) and Zn(II) Ternary Complexes Using Ion Mobility-Mass Spectrometry, JoVE, 2022 e63722.
[13] A.A. Flores, A.V. Arredondo, A.J. Corrales, C.L. Duvak, C.L. Mitchell, O. Falokun, C. L. Aguilar, A. Kim, B.C. Daniel, H.D. Karabulut, R. Spezia, L.A. Angel, Thermochemical and conformational studies of Ni(II) and Zn(II) ternary complexes of alternative metal binding peptides with nitrilotriacetic acid, Int. J. Mass Spectrom. 473 (2022) 116792.
[14] A.A. Flores, O.S. Falokun, A.B. Ilesanmi, A.V. Arredondo, L. Truong, N. Fuentes, R. Spezia, L.A. Angel, Formation of Co(II), Ni(II), Zn(II) complexes of alternative metal binding heptapeptides and nitrilotriacetic acid: Discovering new potential affinity tags, Int. J. Mass Spectrom. 463 (2021) 116554.
[15] R. Vangala, L.A. Angel, ESI-IM-MS reveals the metal binding of three analog methanobactin peptides with different numbers of free Cys at physiological pH, Int. J. Mass Spectrom. 468 (2021) 116640.

[16] E.N. Yousef, L.A. Angel, Comparison of the pH-dependent formation of His and Cys heptapeptide complexes of nickel(II), copper(II), and zinc(II) as determined by ion mobility-mass spectrometry, J. Mass Spectrom. 55 (2020) e4489.
[17] A.B. Ilesanmi, T.C. Moore, L.A. Angel, pH dependent chelation study of Zn(II) and Ni(II) by a series of hexapeptides using electrospray ionization - ion mobility - mass spectrometry, Int. J. Mass Spectrom. 455 (2020) 116369.
[18] E.N. Yousef, R. Sesham, J.W. McCabe, R. Vangala, L.A. Angel, Ion mobility-mass spectrometry techniques for determining the structure and mechanisms of metal ion recognition and redox activity of metal binding oligopeptides, J. Visualized Exp. (2019) e60102.
[19] Y.-F. Lin, E.N. Yousef, E. Torres, L. Truong, J.M. Zahnow, C.B. Donald, Y. Qin, L. A. Angel, Weak acid-base interactions of histidine and cysteine affect the charge states, tertiary structure, and Zn(II)-binding of heptapeptides, J. Am. Soc. Mass Spectrom. 30 (2019) 2068–2081.
[20] S.M. Wagoner, M. Deeconda, K.L. Cumpian, R. Ortiz, S. Chinthala, L.A. Angel, The multiple conformational charge states of zinc(II) coordination by 2His-2Cys oligopeptide investigated by ion mobility - mass spectrometry, density functional theory and theoretical collision cross sections, J. Mass Spectrom. 51 (2016) 1120–1129.
[21] Y. Vytla, L.A. Angel, Applying ion mobility-mass spectrometry techniques for explicitly Identifying the products of Cu(II) reactions of 2His-2Cys Motif peptides, Anal. Chem. 88 (2016) 10925–10932.
[22] D. Choi, A.A. Alshahrani, Y. Vytla, M. Deeconda, V.J. Serna, R.F. Saenz, L.A. Angel, Redox activity and multiple copper(I) coordination of 2His-2Cys oligopeptide, J. Mass Spectrom. 50 (2015) 316–325.
[23] R. Sesham, D.W. Choi, A. Balaji, S. Cheruku, C. Ravichetti, A.A. Alshahrani, M. Nasani, L.A. Angel, The pH dependent Cu(II) and Zn(II) binding behavior of an analog methanobactin peptide, Eur. J. Mass Spectrom. 19 (2013) 463–473.
[24] S.D. Pringle, K. Giles, J.L. Wildgoose, J.P. Williams, S.E. Slade, K. Thalassinos, R. H. Bateman, M.T. Bowers, J.H. Scrivens, An investigation of the mobility separation of some peptide and protein ions using a new hybrid quadrupole/travelling wave IMS/oa-ToF instrument, Int. J. Mass Spectrom. 261 (2007) 1–12.
[25] J.G. Forsythe, A.S. Petrov, C.A. Walker, S.J. Allen, J.S. Pellissier, M.F. Bush, N. V. Hud, F.M. Fernandez, Collision cross section calibrants for negative ion mode traveling wave ion mobility-mass spectrometry, Analyst 14 (2015) 6853–6861.
[26] T. Wu, J. Derrick, M. Nahin, X. Chen, C. Larriba-Andaluz, Optimization of long range potential interaction parameters in ion mobility spectrometry, J. Chem. Phys. 148 (2018) 074102.
[27] J.J.P. Stewart, Optimization of parameters for semiempirical methods V: Modification of NDDO approximations and application to 70 elements, J. Mol. Model. 13 (2007) 1173–1213.
[28] M.J. Frisch, G.W. Trucks, H.B. Schlegel, G.E. Scuseria, M.A. Robb, J.R. Cheeseman, G. Scalmani, V. Barone, B. Mennucci, G.A. Petersson, H. Nakatsuji, M. Caricato, X. Li, H.P. Hratchian, A.F. Izmaylov, J. Bloino, G. Zheng, J.L. Sonnenberg, M. Hada, M. Ehara, K. Toyota, R. Fukuda, J. Hasegawa, M. Ishida, T. Nakajima, Y. Honda, O. Kitao, H. Nakai, T. Vreven, J. Montgomery, A. J, J.E. Peralta, F. Ogliaro, M. Bearpark, J.J. Heyd, E. Brothers, K.N. Kudin, V.N. Staroverov, R. Kobayashi, J. Normand, K. Raghavachari, A. Rendell, J.C. Burant, S.S. Iyengar, J. Tomasi, M. Cossi, N. Rega, J.M. Millam, M. Klene, J.E. Knox, J.B. Cross, V. Bakken, C. Adamo, J. Jaramillo, R. Gomperts, R.E. Stratmann, O. Yazyev, A.J. Austin, R. Cammi, C. Pomelli, J.W. Ochterski, R.L. Martin, K. Morokuma, V.G. Zakrzewski, G.A. Voth, P. Salvador, J.J. Dannenberg, S. Dapprich, A.D. Daniels, Ö. Farkas, J. B. Foresman, J.V. Ortiz, J. Cioslowski, D.J. Fox, Gaussian 09, Revision C.01, Gaussian Inc, Gaussian, Inc, Wallingford CT. Wallingford CT, 2012.
[29] N.F. Dalleska, K. Honma, L.S. Sunderlin, P.B. Armentrout, Solvation of transition metal ions by water. Sequential binding energies of M+(H2O)x (x = 1-4) for M = Ti to Cu determined by collision-induced dissociation, J. Am. Chem. Soc. 116 (1994) 3519–3528.
[30] V.F. DeTuri, K.M. Ervin, Competitive threshold collision-induced dissociation: gas-phase Acidities and bond dissociation energies for a series of Alcohols, J. Phys. Chem. A 103 (1999) 6911–6920.
[31] C. Iceman, P.B. Armentrout, Collision-induced dissociation and theoretical studies of K+ complexes with ammonia: a test of theory for potassium ions, Int. J. Mass Spectrom. 222 (2003) 329–349.
[32] B.D. Balogh, Z. Bihari, P. Buglyo, G. Csire, Z. Kerekes, M. Lukacs, I. Sovago, K. Varnagy, Metal binding selectivity of an N-terminally free multihistidine peptide HAVAHHH-NH2, New J. Chem. 43 (2019) 907–916.
[33] I. Sóvágó, K. Várnagy, N. Lihi, Á. Grenács, Coordinating properties of peptides containing histidyl residues, Coord. Chem. Rev. 327–328 (2016) 43–54.
[34] V. Joszai, I. Turi, C. Kallay, G. Pappalardo, G. Di Natale, E. Rizzarelli, I. Sovago, Mixed metal copper(II)-nickel(II) and copper(II)-zinc(II) complexes of multihistidine peptide fragments of human prion protein, J. Inorg. Biochem. 112 (2012) 17–24.
[35] H. Kozlowski, B. Decock-Le Reverend, D. Ficheux, C. Loucheux, I. Sovago, Nickel (II) complexes with sulfhydryl containing peptides. Potentiometric and spectroscopic studies, J. Inorg. Biochem. 29 (1987) 187–197.
[36] M. Lukacs, D. Csilla Palinkas, G. Szunyog, K. Varnagy, Metal binding ability of small peptides containing cysteine residues, ChemistryOpen 10 (2021) 451–463.
[37] N. Lihi, M. Lukacs, D. Szucs, K. Varnagy, I. Sovago, Nickel(II), zinc(II) and cadmium(II) complexes of peptides containing separate aspartyl and cysteinyl residues, Polyhedron 133 (2017) 364–373.
[38] M. Raics, N. Lihi, A. Laskai, C. Kallay, K. Varnagy, I. Sovago, Nickel(II), zinc(II) and cadmium(II) complexes of hexapeptides containing separate histidyl and cysteinyl binding sites, New J. Chem. 40 (2016) 5420–5427.
[39] G. Csire, I. Turi, I. Sovago, E. Karpati, C. Kallay, Complex formation processes and metal ion catalyzed oxidation of model peptides related to the metal binding site of the human prion protein, J. Inorg. Biochem. 203 (2020) 110927.
[40] P. Gockel, M. Gelinsky, R. Vogler, H. Vahrenkamp, Solution behaviour and zinc complexation of tripeptides with cysteine and/or histidine at both termini, Inorg. Chim. Acta. 272 (1998) 115–124.